CHAPTER 6

TRIBOLOGICAL BEHAVIOUR

In this chapter, the tribological behaviour of the indigenously developed bainitic steels and pearlitic steels of the same compositions is discussed. This chapter provides variation in mass loss, specific wear rate coefficient of friction, worn surface morphology, EDS analysis, and worn surface roughness, subsurface microstructure, hardening behaviour of worn surface

6.1 MASS LOSS

The variations of mass losses with sliding distance at different applied normal loads are depicted in Figures 6.1 to 6.3 for austempered and patented steel pins. The mass losses are increased with the sliding distance and also with the application of higher normal load in the case of bainitic steels B12VA-1, B12VA-2, B14VA-1, B14VA-2, B15VA-1 and B15VA-2 (Figures 6.1a-b, 6.2a-b and 6.3a-b).

The mass loss of B12VA-1 is slightly greater than that of B12VA-2. Similarly, the mass loss of B14VA-1 and B15VA-1 are somewhat higher than that of B14VA-2 and B15VA-2, respectively. The mass losses for 10 N and 20 N applied normal loads are quite similar and lesser but abruptly increased when normal load increases from 30 N.

Figures 6.1c, 6.2c and 6.3c depict the mass loss variation with sliding distance against applied normal loads for pearlitic pins P12VA, P14VA and P15VA. The mass losses are increased with sliding distance uniformly till 30 N normal load. The mass losses increase as the load increases from 30 to 40 N enormously till 3000 m of sliding distance but thereafter it decreases slightly at 4500 m and again it increases for 6000 m sliding distance. This trend is observed in all the pearlitic pins.

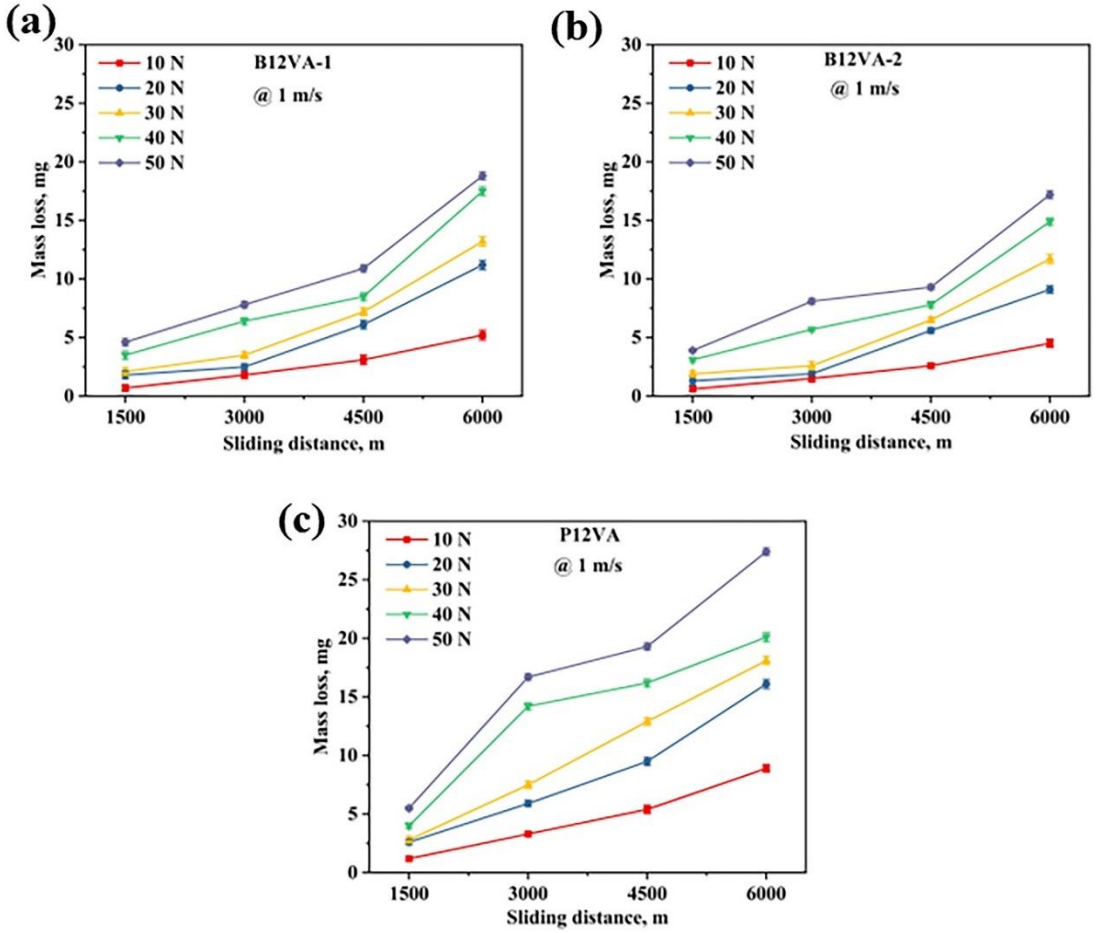

Figure 6.1 Variation of mass loss vs sliding distances at different normal loads: (a) B12VA-1, (b) B12VA-2, and (c) P12VA.

The B14VA-1 pins reveal much higher mass losses among austempered steel (bainitic pins) and P14VA pins depict slightly greater mass losses among the pearlitic pins. The pearlitic pin P14VA shows higher mass losses among the austempered and patented steels.

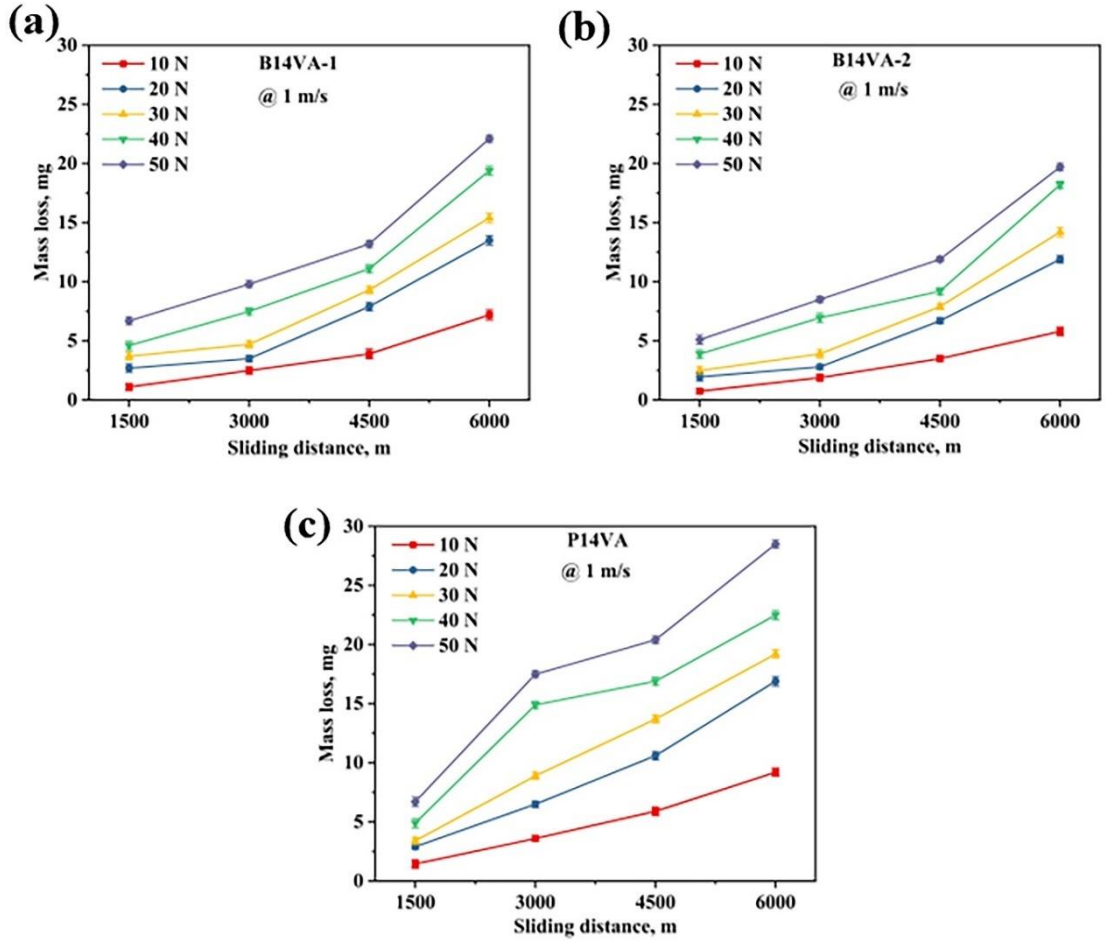

Figure 6.2 Variation of mass loss vs sliding distances at different normal loads: (a) B14VA-1, (b) B14VA-2, and (c) P14VA.

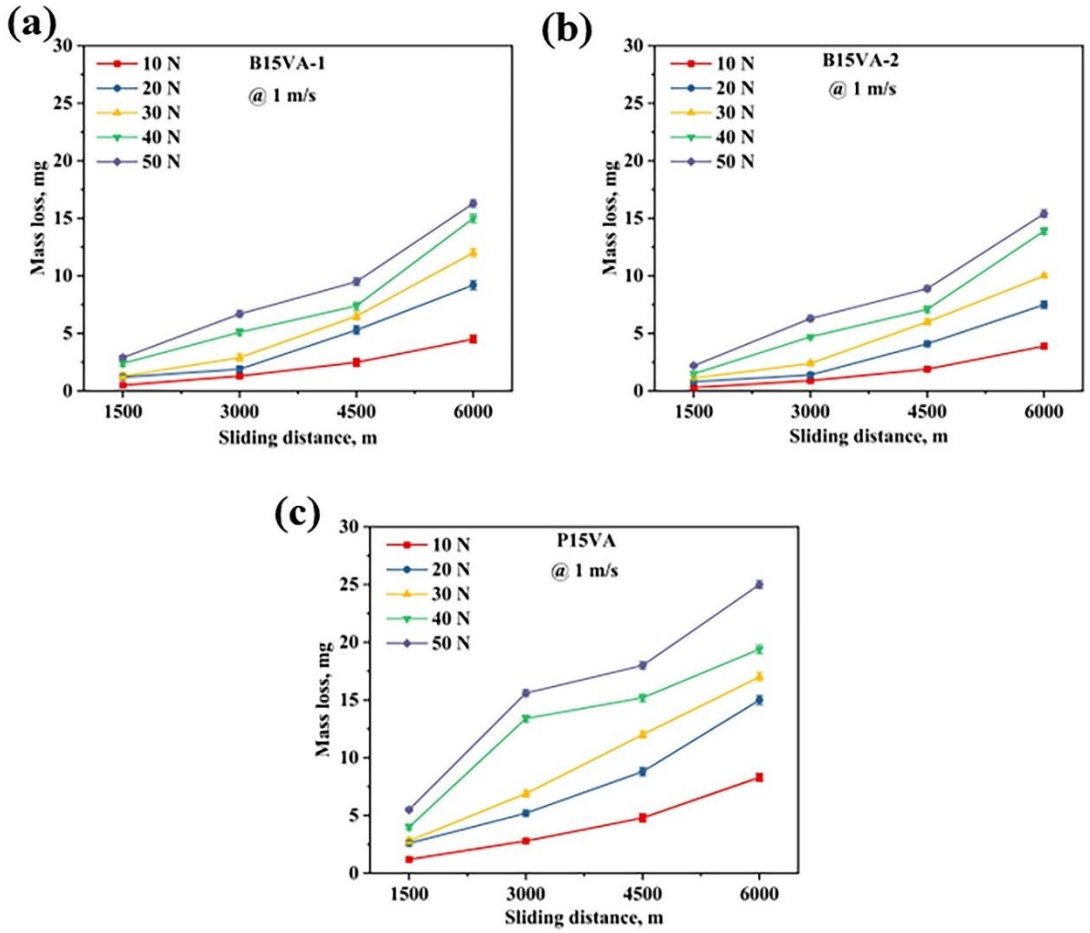

Figure 6.3 Variation of mass loss vs sliding distances at different normal loads: (a) B15VA-1, (b) B15VA-2, and (c) P15VA.

6.2 SPECIFIC WEAR RATE AND COEFFICIENT OF FRICTION

The specific wear rates of the steels are calculated for 10, 30 and 50 N with the variation of sliding distances and depicted in Figures 6.4 to 6.6. Figure 6.4a displays the specific wear rate of steels at 10 N load and it is observed that trend of specific wear rate is similar for all the steels B12VA-1, B12VA-2 and P12VA. In bainitic steel samples, B12VA-1 shows higher specific wear rate than B12VA-2. The specific wear rate of P12VA is highest among B12VA-1, B12VA-2 and P12VA at 10 N load. Figure 6.4b depicts the trend of specific wear rate at 30 N which is quite similar to that of at 10 N. The specific wear rates at 50 N normal load are displayed in Figure 6.4c which depicts

the higher specific wear rate than that at 10 N and 30 N. Similar type of behaviour is observed in B14VA alloy (B14VA-1, B14VA-2 and P14VA) and B15VA alloy (B15VA-1, B15VA-2 and P15VA) shown in Figure 6.5a-c and Figure 6.6a-c, respectively. Material B14VA-1 reveals highest specific wear rate among the austempered samples and P14VA steel depicts significantly higher specific wear rate amongst the patented steels and also, P14VA steel shows highest specific wear rate among the austempered and patented steels.

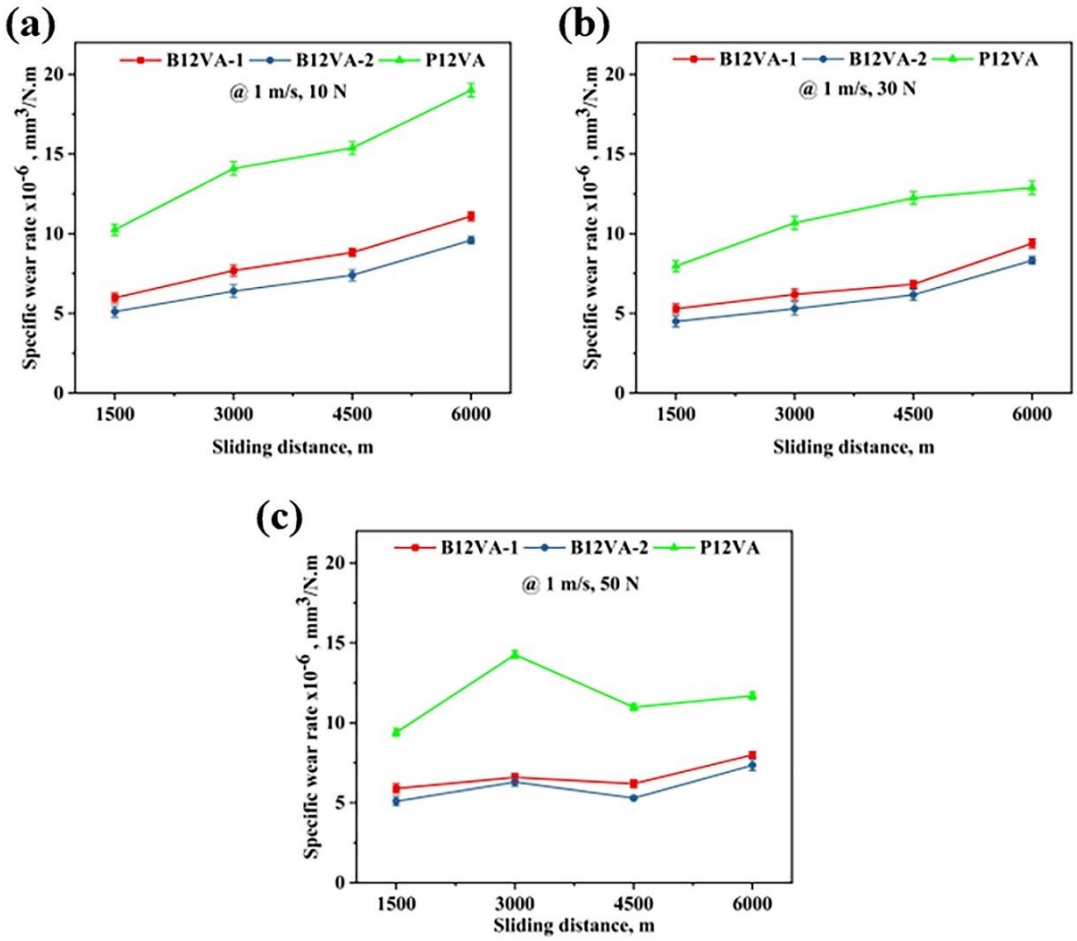

Figure 6.4 Variation of specific wear rate versus sliding distance for B12VA-1, B12VA-2 and P12VA at various applied loads: (a) 10 N, (b) 30 N, and (c) 50 N.

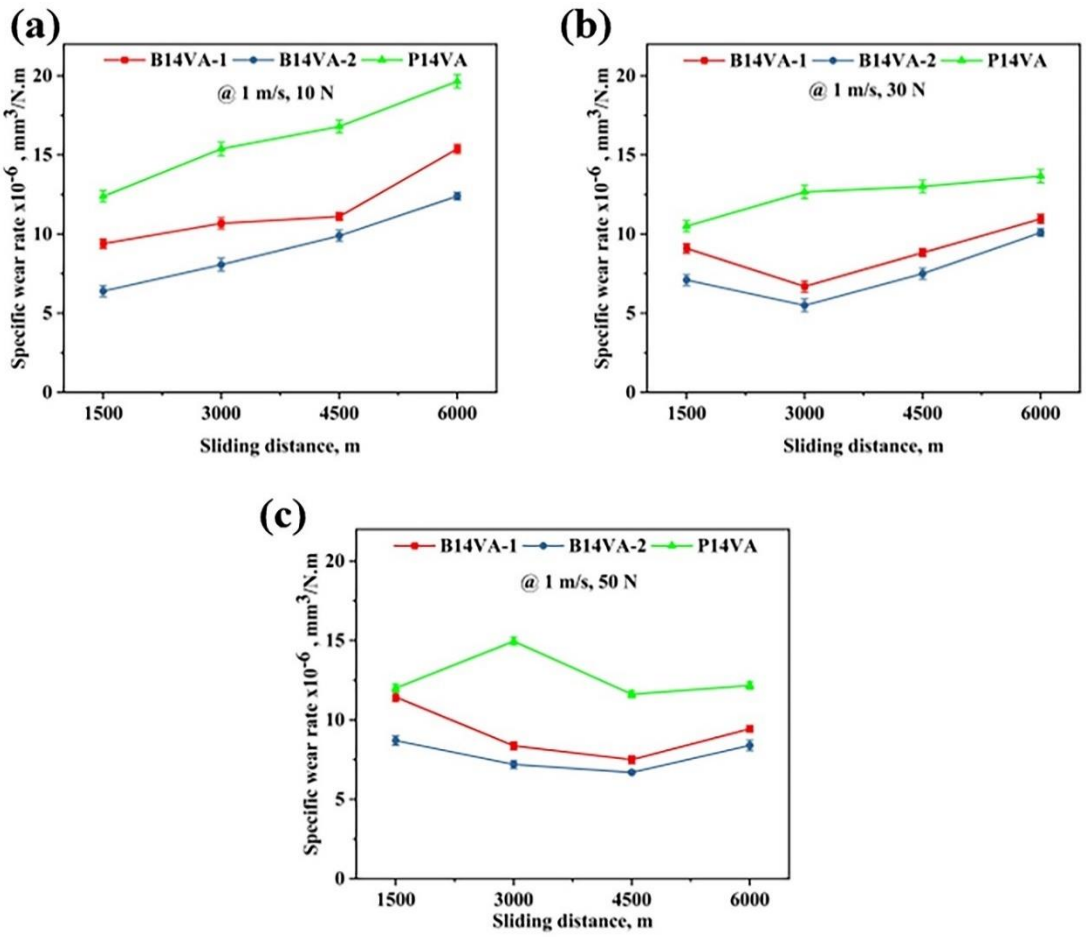

Figure 6.5 Variation of specific wear rate versus sliding distance for B14VA-1, B14VA-2 and P14VA at various applied loads: (a) 10 N, (b) 30 N, and (c) 50 N.

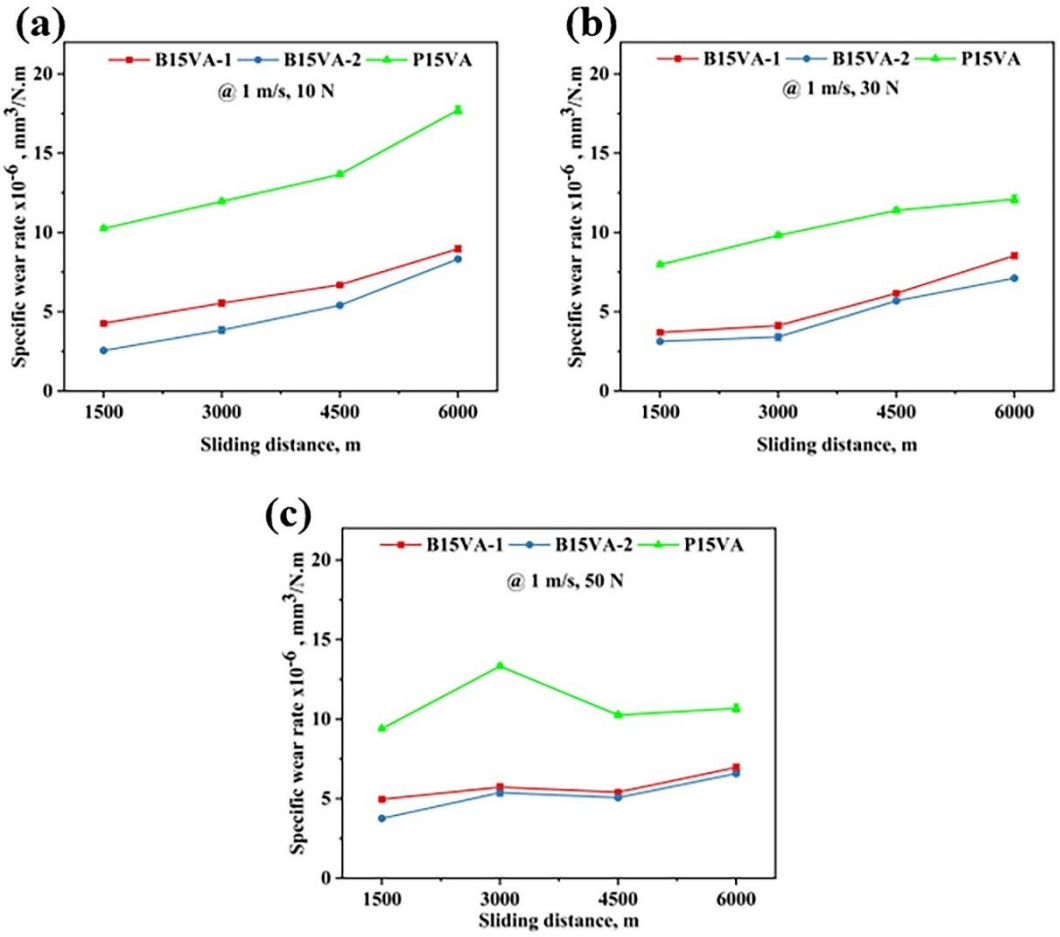

Figure 6.6 Variation of specific wear rate versus sliding distance for B15VA-1, B15VA-2 and P15VA at various applied loads: (a) 10 N, (b) 30 N, and (c) 50 N.

The variations of coefficient of friction (CoF) with sliding period are depicted in Figures 6.7 to 6.9 for the steels. Figure 6.7a shows the coefficient of friction of B12VA-1 at normal loads of 10, 30 and 50 N and the average values are 0.69±0.02, 0.65±0.03 and 0.58±0.02 respectively, and decreases with increase in applied load. The CoF of B12VA-2 at 10, 30 and 50 N are 0.61±0.03, 0.57±0.02 and 0.48±0.03, respectively and also similar trend is observed in B12VA-1 (Figure 6.7b). Figure 6.7c depicts the CoF of P12VA as 0.77±0.07, 0.72±0.02 and 0.58±0.02 at applied loads of 10, 30 and 50 N, respectively. Pearlitic sample also reveals similar trend of decreasing CoF with increasing loads as bainitic steels.

Figure 6.8a depicts the coefficient of friction of B14VA-1 under normal loads of 10, 30, and 50 N, with average values of 0.74±0.03, 0.63±0.04, and 0.62±0.03, respectively, which decrease as the applied load increases. At 10, 30, and 50 N load, the CoF of B14VA-2 is 0.70±0.02, 0.66±0.05, and 0.51±0.03, respectively, and a similar trend is observed for B14VA-1 (Figure 6.8b). Figure 6.8c depicts the CoF of P14VA at applied normal load of 10, 30, and 50 N as 0.81±0.02, 0.75±0.02, and 0.67±0.03, respectively. As with bainitic steels, pearlitic samples exhibit a decreasing CoF with increasing applied load.

Figure 6.9a shows the coefficient of friction of B15VA-1 at normal loads of 10, 30 and 50 N and the average values are 0.65±0.05, 0.61±0.03 and 0.61±0.02 respectively, and reductions with rise in applied load. The CoF of B15VA-2 at 10, 30 and 50 N are 0.66±0.02, 0.55±0.02 and 0.45±0.08, respectively and also similar trend is observed in B15VA-1 (Figure 6.9b). Figure 6.9c depicts the CoF of P15VA as 0.81±0.03, 0.62±0.02 and 0.44±0.02 at applied loads of 10, 30 and 50 N, respectively. Pearlitic sample also reveals similar trend of decreasing CoF with increasing loads as bainitic steels.

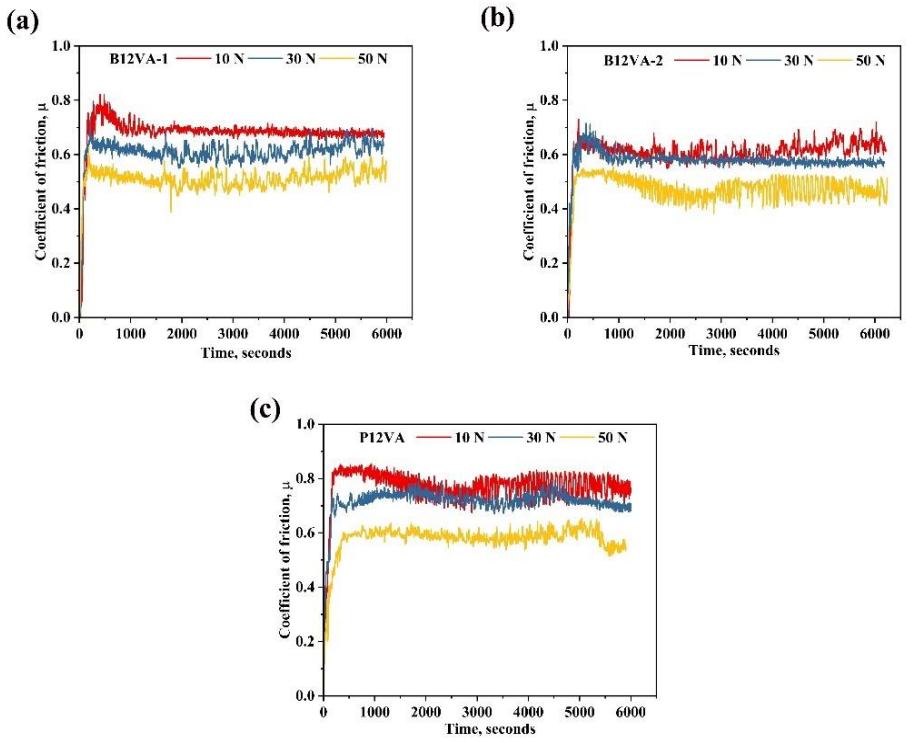

Figure 6.7 The fluctuation of CoF with sliding time for (a) B14VA-1, (b) B14VA-2, and (c) P14VA under varying normal loads.

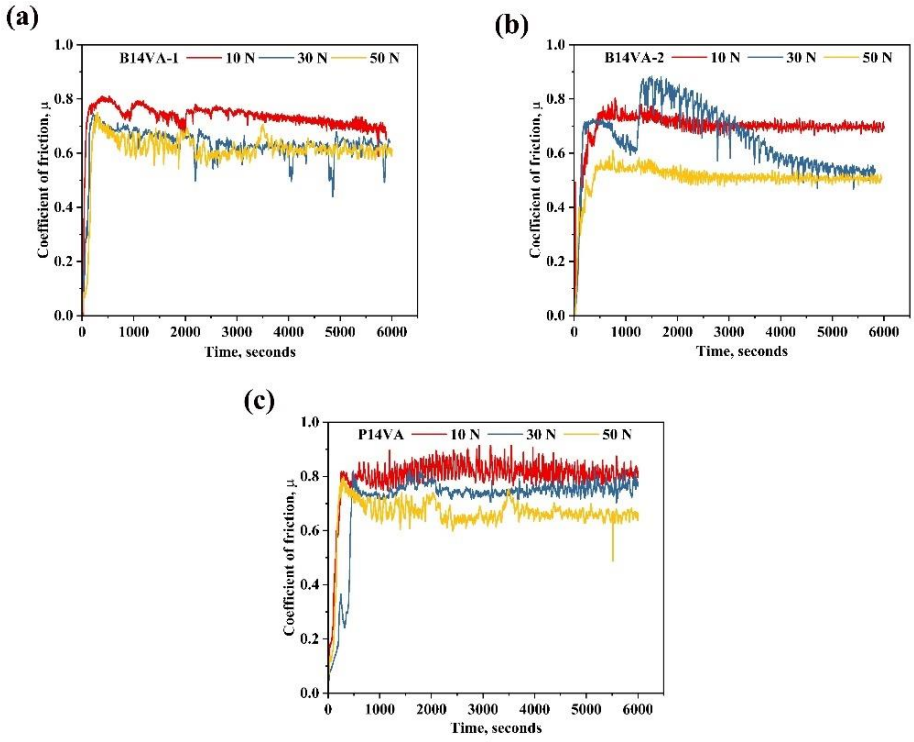

Figure 6.8 The fluctuation in CoF with sliding time for (a) B14VA-1, (b) B14VA-2, and (c) P14VA under varying normal loads.

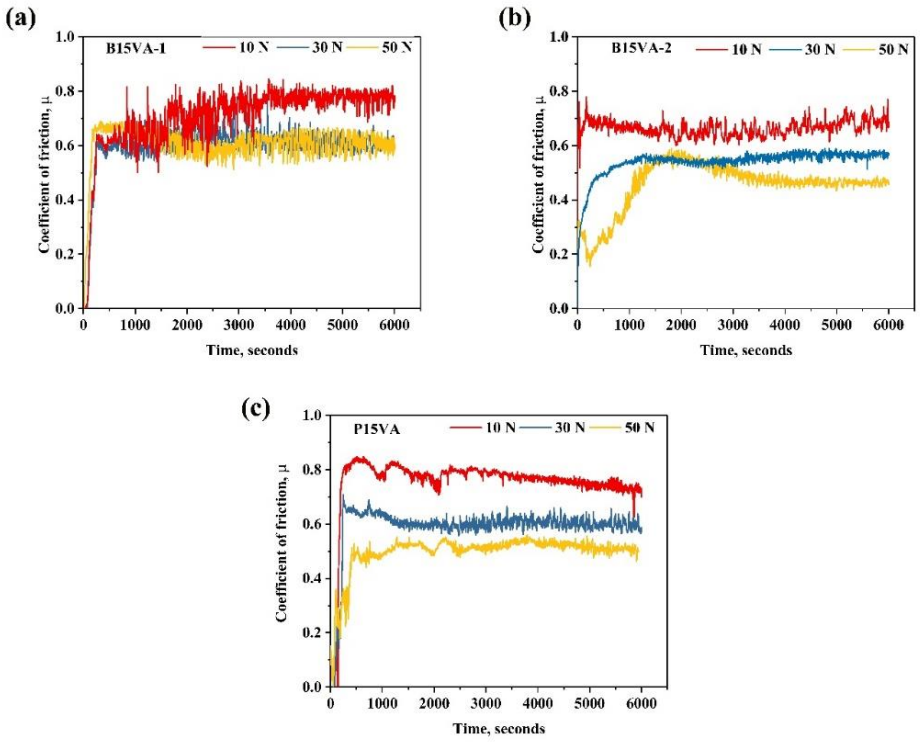

Figure 6.9 The fluctuation in CoF with sliding time for (a) B15VA-1, (b) B15VA-2, and (c) P15VA under varying normal loads.

Table 6.1 Average value of coefficient of friction at different load.

Load	B12 VA-1	B12 VA-2	P12 VA	B14 VA-1	B14 VA-2	P14 VA	B15 VA-1	B15 VA-2	P15 VA
10 N	0.69± 0.02	0.61± 0.03	0.77± 0.07	0.74± 0.03	0.70± 0.02	0.81± 0.02	0.65± 0.05	0.66± 0.02	0.81± 0.02
30 N	0.65± 0.03	0.58± 0.02	0.72± 0.02	0.63± 0.04	0.66± 0.05	0.75± 0.02	0.61± 0.03	0.55± 0.02	0.62± 0.03
50 N	0.58± 0.02	0.48± 0.03	0.58± 0.02	0.62± 0.03	0.51± 0.03	0.67± 0.03	0.61± 0.02	0.45± 0.08	0.47± 0.02

6.3 WORN SURFACE MORPHOLOGY AND EDS ANALYSIS

Worn surfaces of bainitic pins of B12VA-1 after sliding distance of 6000 m at applied loads of 10, 30 and 50 N are displayed in Figure 6.10a, b, and c, respectively. It is observed that deep ploughing groves appear in case of 10 N load (Figure 6.10a), and with rise in load the valley of the groves decreases and also adhesion joints are noted in case of 30 N load (Figure 6.10b). Further increase in load leads to smoother surface along

with adhesion joints (Figure 6.10c). Figure 6.10d-f depicts the SEIs of worn surfaces of B12VA-2 pins after sliding distance of 6000 m under loads of 10, 30 and 50 N, respectively. Similar types of worn morphologies are observed as in B12VA-1 but less smooth surfaces are seen at 50 N. The SEIs of worn surfaces of P12VA pins at 10, 30 and 50 N are depicted in Figure 6.10g-i and formation of deep and wide ploughing groves is seen at 10 N load. Further increase in load results in formation of intense adhesion joints along with oxidative regimes. At 50 N applied load deep ploughing pits are visible (Figure 6.10i).

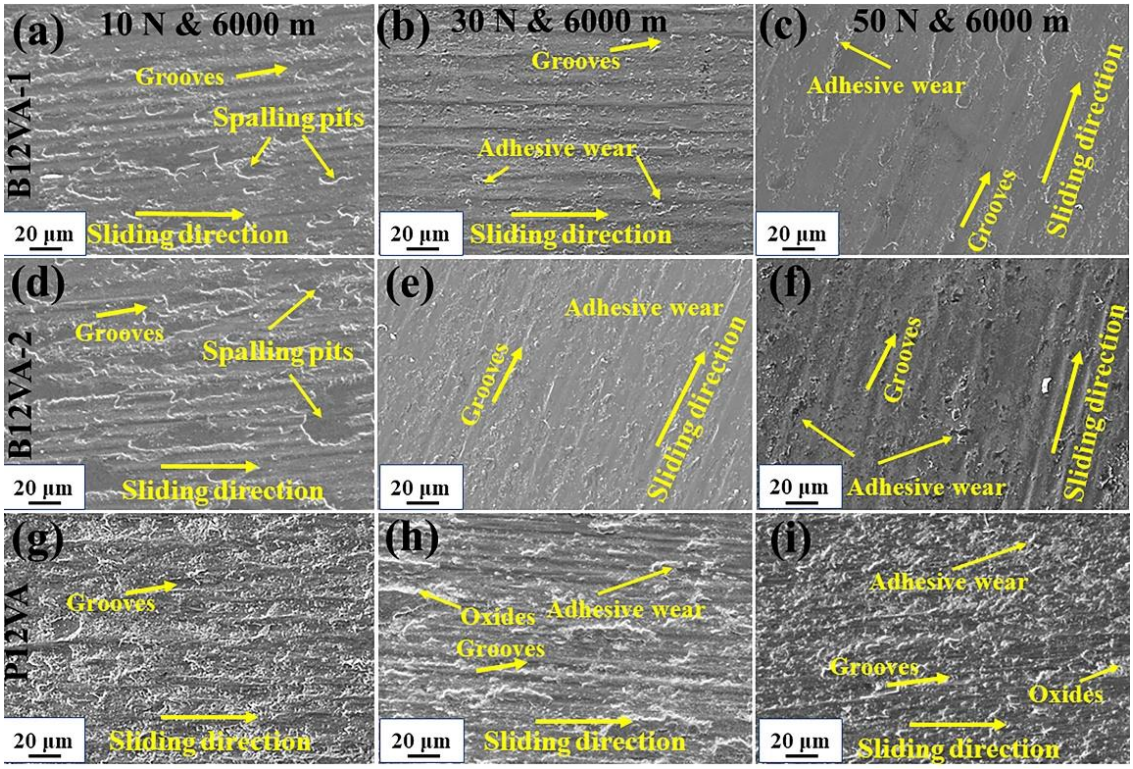

Figure 6.10 SEM SEIs of worn surfaces after 6000m of sliding against tungsten carbide rotating disc at different loads, 10, 30 and 50 N, respectively: (a), (b) &(c) for B12VA-1, (d) (e) & (f) for B12VA-2 and (g), (h) & (i) for P12VA samples.

Figure 6.11a, b, and c depict the worn surfaces of bainitic pins of B14VA-1 after a sliding distance of 6000 m under applied normal load of 10, 30, and 50 N, respectively. Deep abrasive groves are observed at a load of 10 N (Figure 6.11a), and as the load

increases, the valley of the groves decreases and adhesion joints appear at a load of 30 N (Figure 6.11b). Increasing the burden further results in a smoother surface and adhesion junctions (Figure 6.11c). Figure 6.11d-f illustrates the SEIs of worn surfaces of B14VA-2 pins after 6000 m of sliding under stresses of 10, 30, and 50 N, respectively. Similar kinds of worn morphologies are observed, but there are fewer flat surfaces at 50 N compared to B14VA-1. Figure 6.11g-i depicts the SEIs of eroded surfaces of P14VA pins under loads of 10, 30, and 50 N, with 10 N causing the formation of deep and wide ploughing groves. Further increase in load leads to the formation of intense adhesion joints and oxidative regimes. Deep ploughing trenches are visible at 50 N applied load (Figure 6.11i).

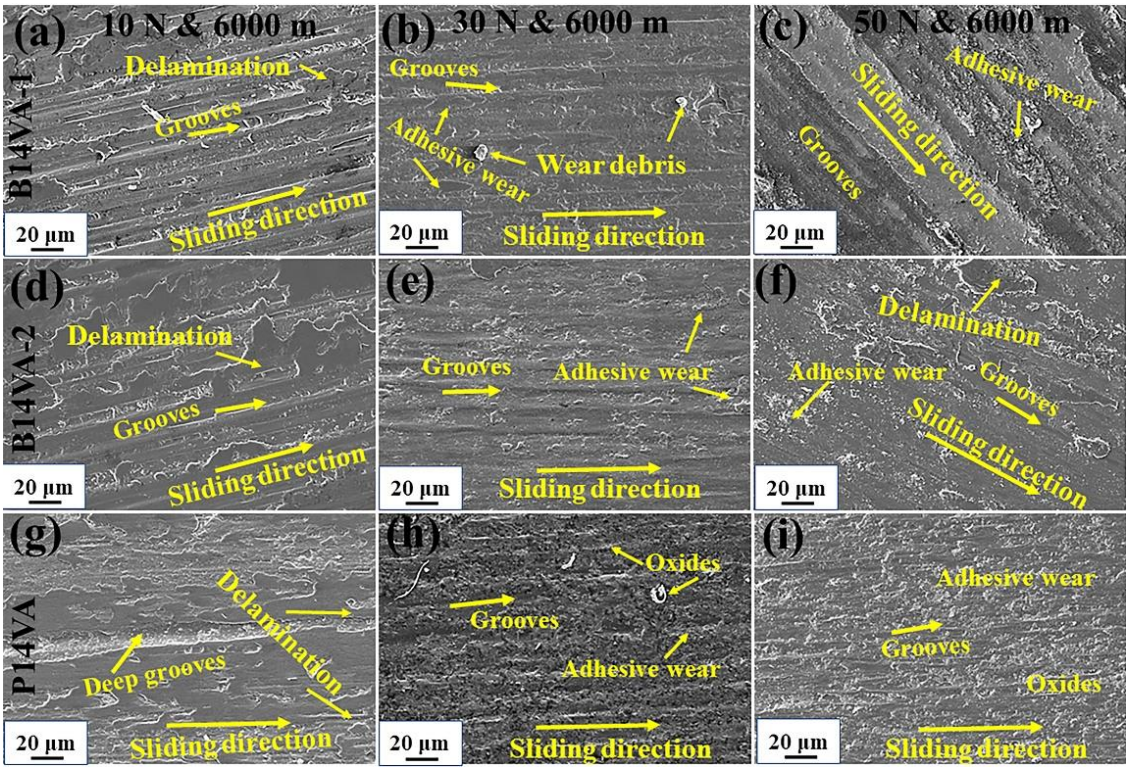

Figure 6.11 SEM SEIs of worn surfaces after 6000m of sliding against tungsten carbide rotating disc at different loads, 10, 30 and 50 N, respectively: (a), (b) &(c) for B14VA-1, (d) (e) & (f) for B14VA-2 and (g), (h) & (i) for P14VA samples.

Worn surfaces of bainitic pins of B15VA-1 after sliding distance of 6000 m at normal loads of 10 N, 30 N and 50 N are displayed in Figure 6.12a, b, and c, respectively. It is observed that deep ploughing groves appear in case of 10 N load (Figure 6.12a), and with rise in load the valley of the groves decreases and also adhesion joints are there in case of 30 N load (Figure 6.12b). Further increase in load leads to smoother surface along with adhesion joints (Figure 6.12c). Figure 6.12d-f depicts the SEIs of worn surfaces of B15VA-2 pins after sliding distance of 6000 m under loads of 10 N, 30 N and 50 N, respectively. Similar types of worn morphologies are observed as in B15VA-1 but less smooth surfaces are seen at 50 N. The SEIs of worn surfaces of P15VA pins at 10 N, 30 N and 50 N are depicted in Figure 6.12g-i and formation of deep and wide ploughing groves is seen at 10 N load. Further increase in load results in formation of intense adhesion joints along with oxidative regimes. At 50 N applied load deep ploughing pits are visible (Figure 6.12i).

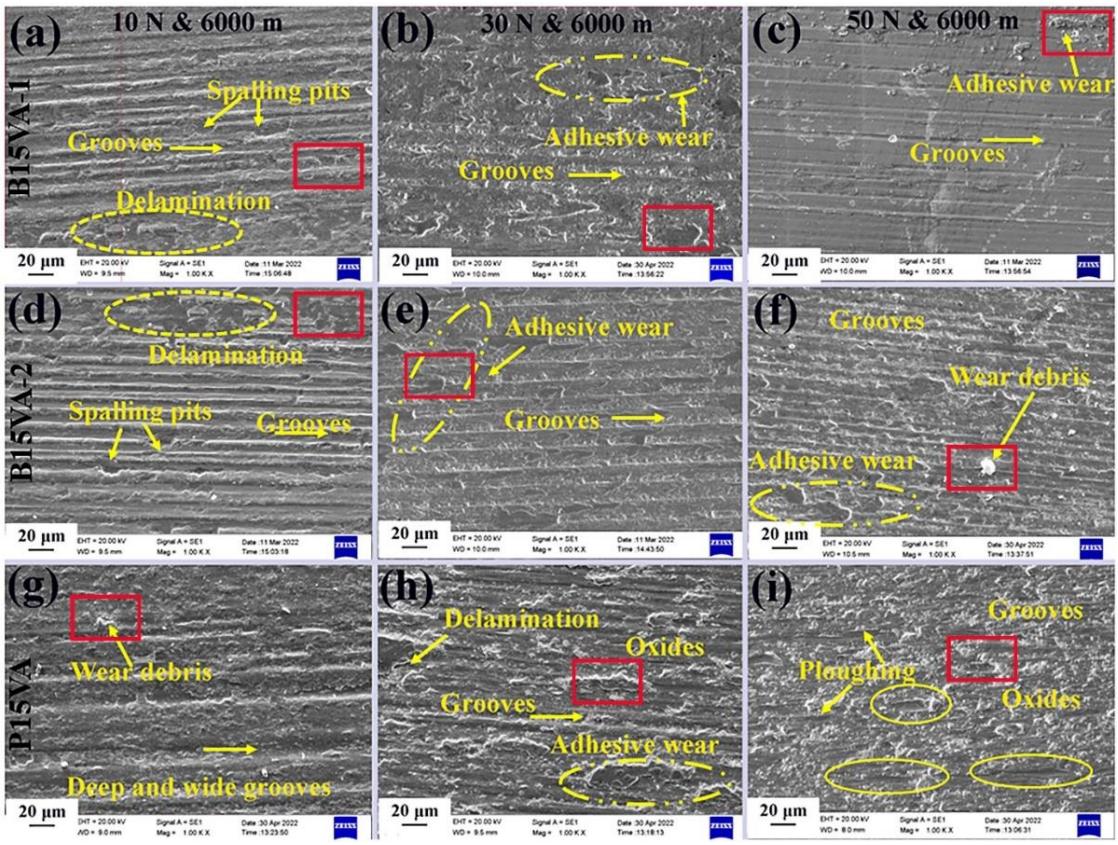

Figure 6.12 SEM SEIs of worn surfaces after 6000m of sliding against tungsten carbide rotating disc at different loads, 10, 30 and 50 N, respectively: (a), (b) &(c) for B15VA-1, (d) (e) & (f) for B15VA-2 and (g), (h) & (i) for P15VA samples.

The SEM EDS analysis of the worn surface marked by red colour rectangle on Figure 6.12a-i are depicted in the corresponding Figure 6.13a-i. From EDS analysis, it is observed that there is no evidence of counter disc material but at lower loads Fe_3O_4 forms on the other hand at higher load it confirms the formation of both Fe_3O_4 and Fe_2O_3 oxides. Figure 6.14 shows the SEM SEIs and EDS analysis of wear debris of bainitic and pearlitic pins of B15VA alloy sliding against tungsten carbide disc. Figure 6.14a depicts the SEM SEI of wear debris of B15VA-2 after sliding distance of 6000 m at 50 N load and corresponding energy dispersive spectroscopy analysis of marked region 1 and 2 of Figure 6.14a are depicted in Figure 6.14b & c, respectively. From energy dispersive spectroscopy analysis, it was observed that good amount of oxides of iron are formed

during sliding. SEM SEI and corresponding energy dispersive spectroscopy analysis of marked region 3 and 4 are depicted in Figure 6.14d-f, respectively. It shows that much higher amount of oxides than that of bainitic pins were forming in pearlitic pins. The energy dispersive spectroscopy analysis of wear debris revealed negligible amount of counter disc material.

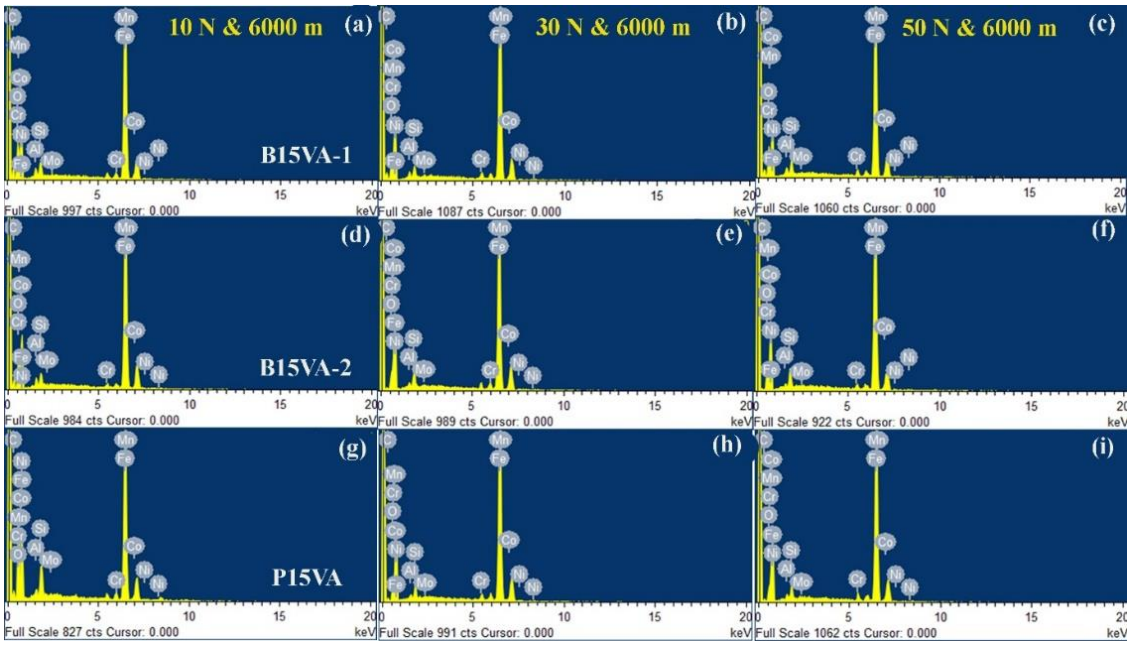

Figure 6.13 Energy dispersive spectroscopy analysis of worn surfaces after 6000m of sliding against tungsten carbide rotating disc at loads of 10, 30 and 50 N, respectively: (a), (b) &(c) for B15VA-1, (d), (e) &(f) for B15VA-2 and (g), (h) & (i) for P15VA.

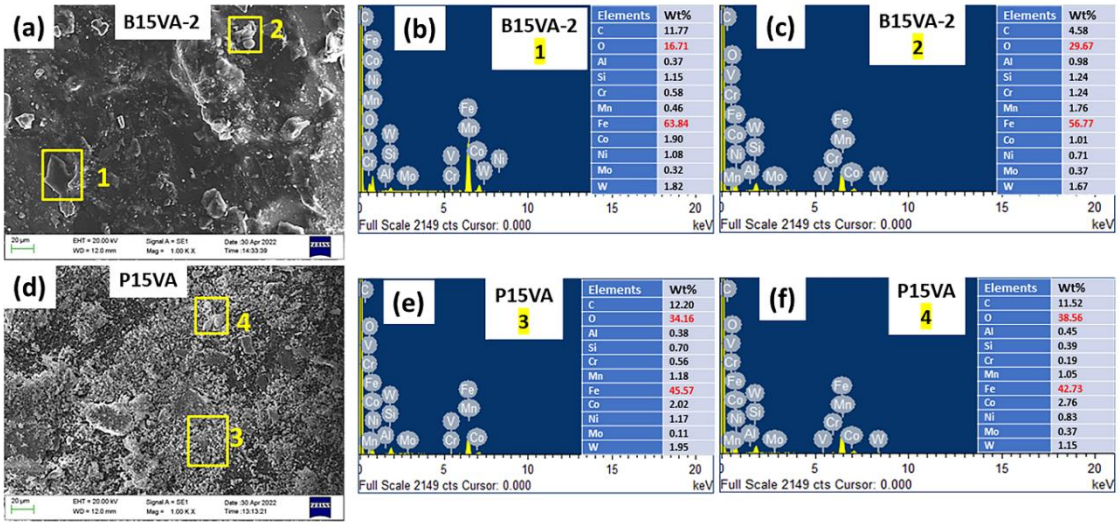

Figure 6.14 SEM energy dispersive spectroscopy analysis of wear debris after sliding distance of 6000 m at 50 N load (a) SEM SEI of B15VA-2, (b) EDS analysis of marked region 1, (c) EDS analysis of marked region 2, (d) SEM SEI of P15VA, (e) EDS analysis of marked region 3 and (f) EDS analysis of marked region 4.

6.4 SURFACE ROUGHNESS MEASUREMENT

Figure 6.15a-i depicts the 3D profile of the worn surfaces of the steels after 6000 m of sliding distance under load of 10, 30, and 50 N, using atomic force microscopy. The peak width (~16 µm to ~5 µm) and peak/valley ratio of ±1 µm to ±150 nm of the worn surfaces of B15VA-1 decreases with rise in load from 10 to 50 N (Figure 6.15a-c). Similarly, for B15VA-2, the peak width decreases from ~15 µm to ~6 µm and peak/valley ratio decreases from ±1 µm to ±200 nm (Figure 6.15d-f). The peak width of worn surfaces of patented steel pins (P15VA) reduces from 18 µm to 9 µm and depth of peak/valley decreases from ±2.5 µm to ±1 µm (Figure 6.15g-i). It is observed that increase in applied normal load leads to smoother surface.

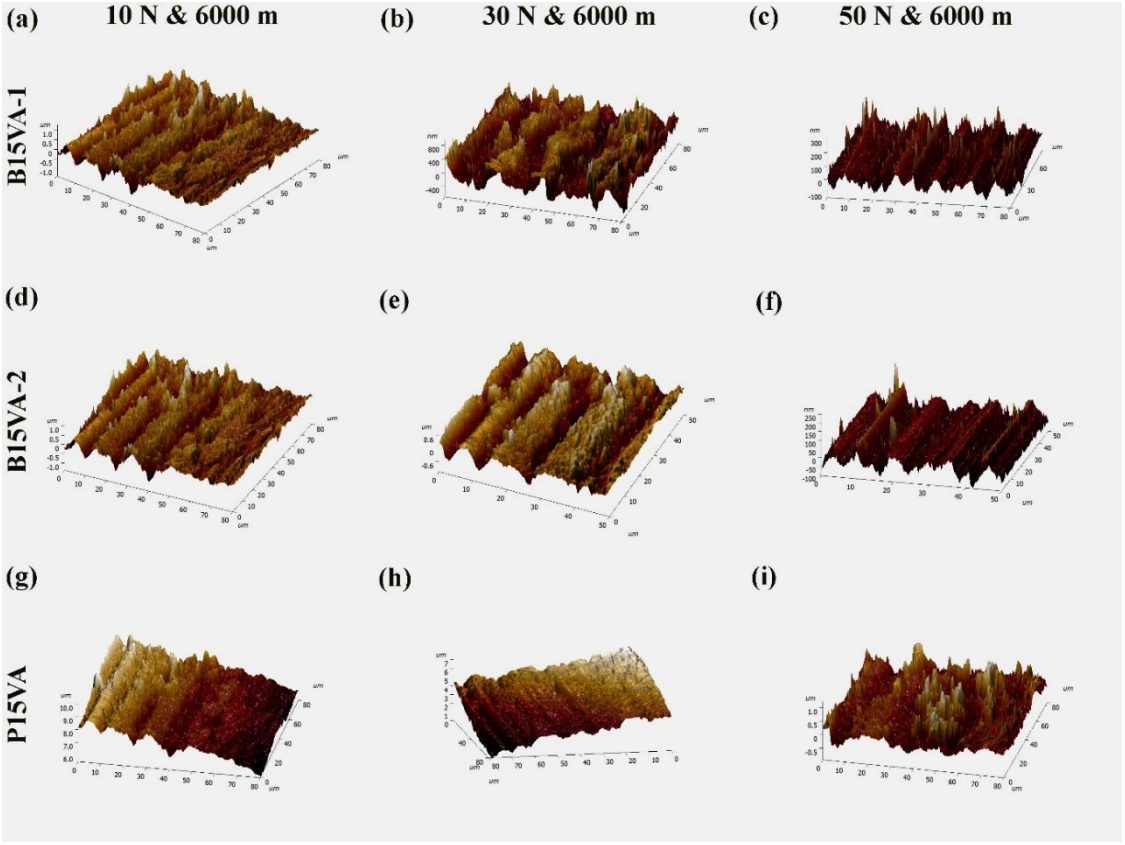

Figure 6.15 AFM analysis of the worn surfaces after 6000m of sliding against tungsten carbide rotating disc at various loads of 10, 30 and 50 N, respectively: (a), (b) &(c) for B15VA-1, (d) (e) & (f) for B15VA-2 and (g), (h) & (i) for P15VA.

The values of average roughness of the worn-out surfaces of B12VA, B14VA and B15VA alloys are depicted in Figures 6.16 to 6.18, measured by stylus profile surface roughness tester. Figure 6.16a depicts the plots of average roughness versus sliding distance for loads of 10 N, 30 N, and 50 N. It can be seen that the average roughness value for B12VA-1 pins at a load of 10 N decreases from 5.8±0.4 μm to 4.6±0.6 μm as the sliding distance increases. It decreases from 4.6±0.5 μm to 3.6±0.4 μm as the applied load increases from 10 N to 50 N at a sliding distance of 6000 meters. Also, B12VA-2 pins exhibit comparable average roughness values (Figure 6.16b). In addition, the average roughness values of patented steel pins (P12VA) decrease as load and sliding distance increase. At a load of 10 N, its value is 6.6±0.6 μm, and increasing the load to

50 N decreases the average roughness to 4.9±0.4 µm (Figure 6.16c). It appears that the surface roughness values of patented steel pins were greater than those of austempered steel pins.

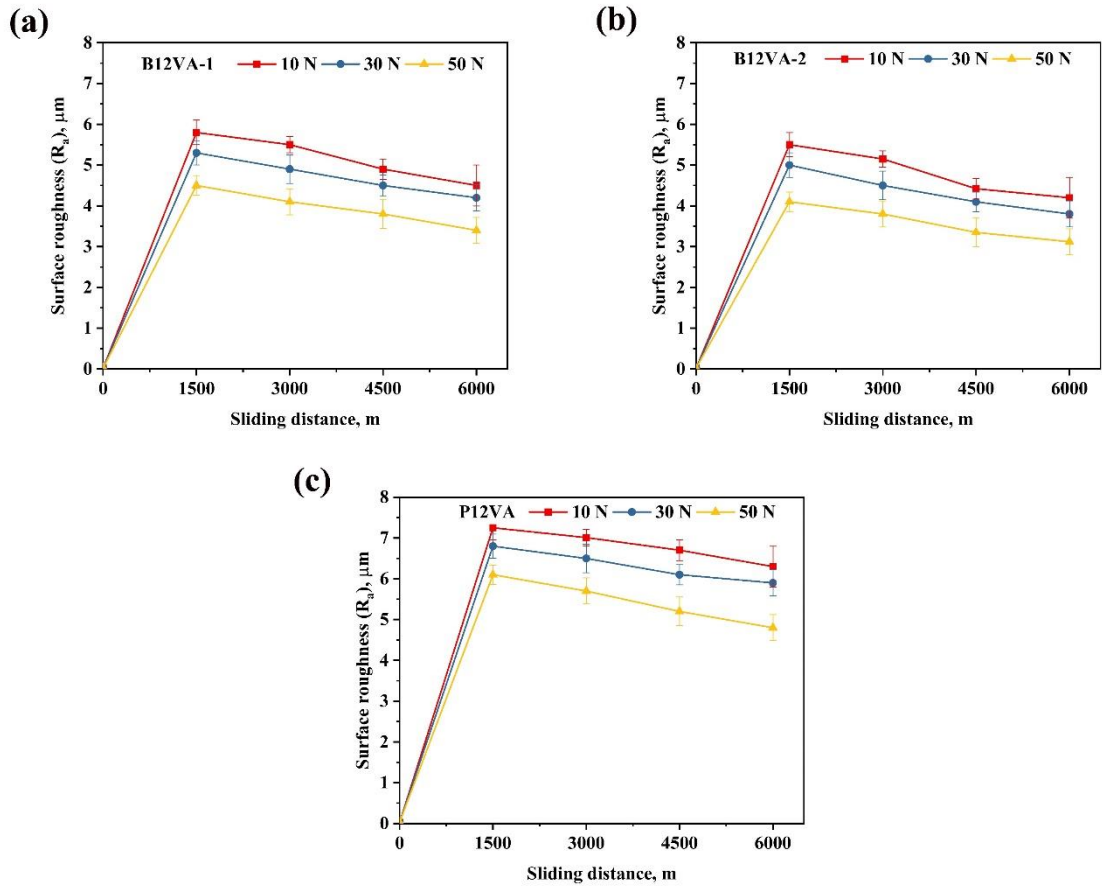

Figure 6.16 Variation of surface roughness of worn surfaces with sliding distance at different normal loads: (a) B12VA-1, (b) B12VA-2 and (c) P12VA.

Figure 6.17a shows average roughness vs sliding distance for applied normal loads of 10 N, 30 N, and 50 N. As sliding distance rises, the average roughness value for B14VA-1 pins at 10 N drops from 6.8±0.4 µm to 5.9±0.5 µm. At 6000 meters and 10 N to 50 N load, it drops from 5.9±0.4 µm to 4.5±0.3 µm. B14VA-2 pins depicts average roughness value of 4.6±0.4 µm and decreased to 3.1±0.3 µm with increase in load to 50 N (Figure 6.17b). As load and sliding distance rise, patented steel pins (P14VA) average

roughness decreases. Average roughness is 6.6±0.6 µm at 10 N and 5.1±0.4 µm at 50 N (Figure 6.17c). Patented steel pins have more surface roughness than austempered ones.

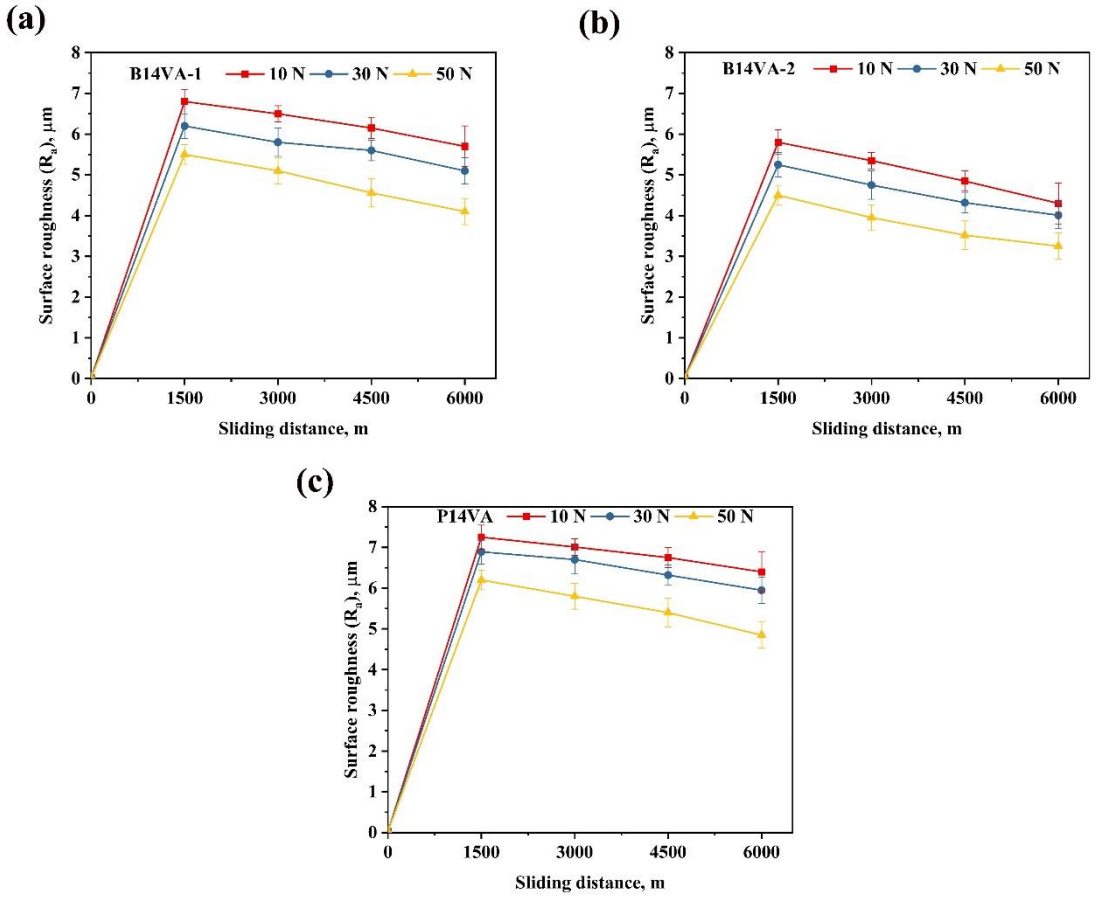

Figure 6.17 Variation of surface roughness of worn surfaces with sliding distance at different normal loads: (a) B14VA-1, (b) B14VA-2 and (c) P14VA.

Figure 6.18a shows the plots of average roughness vs sliding distance at 10 N, 30 N and 50 N loads for B15VA-1 and it is observed that average roughness value decreases from 4.9±0.3 µm to 4.2±0.5 µm with sliding distance for B15VA-1 pins at load of 10 N. It is also reduced with rise in applied load from 4.2±0.5 µm to 2.53±0.32 µm with rise in load from 10 to 50 N at 6000 m sliding distance. Also, similar average roughness values are observed for B15VA-2 pins (Figure 6.18b). The average roughness values for patented steel pins also reduces with increase in load and sliding distance. At 10 N load,

its value is 6.15±0.5 μm and further increase in load to 50 N reduces average roughness to 4.6±0.32 μm (Figure 6.18c). It seems patented steel pins exhibited higher roughness values than that of austempered pins.

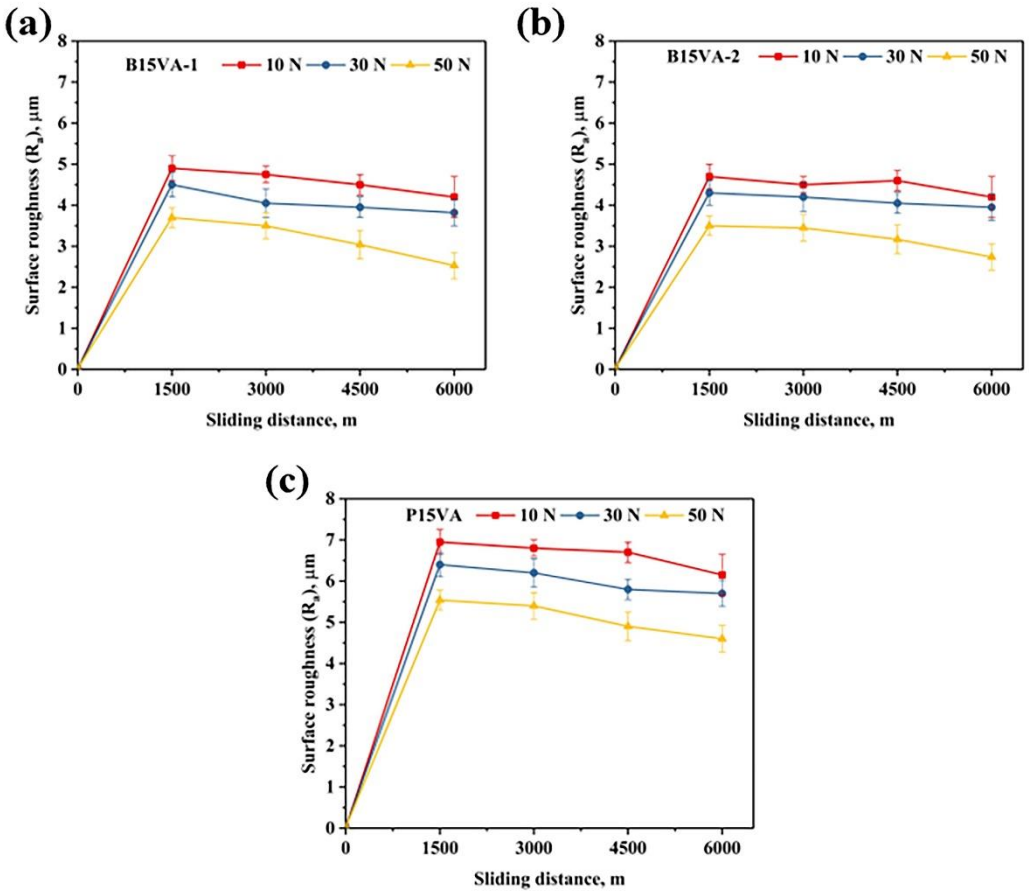

Figure 6.18 Variation of surface roughness of worn surfaces with sliding distance at different normal loads: (a) B15VA-1, (b) B15VA-2 and (c) P15VA.

6.5 SUB-SURFACE MICROSTRUCTURAL CHARACTERIZATION BY TEM

The subsurface TEM BFI and SADP of the worn surface of B15VA-1 is depicted in the Figure 6.19. The BFI confirms the formation of nanostructured bainite, retained austenite along with new phase "strain-induced martensite (epsilon type, ε_m)" during pin-on-disk sliding wear for 6000 m sliding distance at 50 N normal load. The SADP confirmed the existence of epsilon martensite, nanostructured bainite and retained austenite (shown in inset of Figure 6.19).

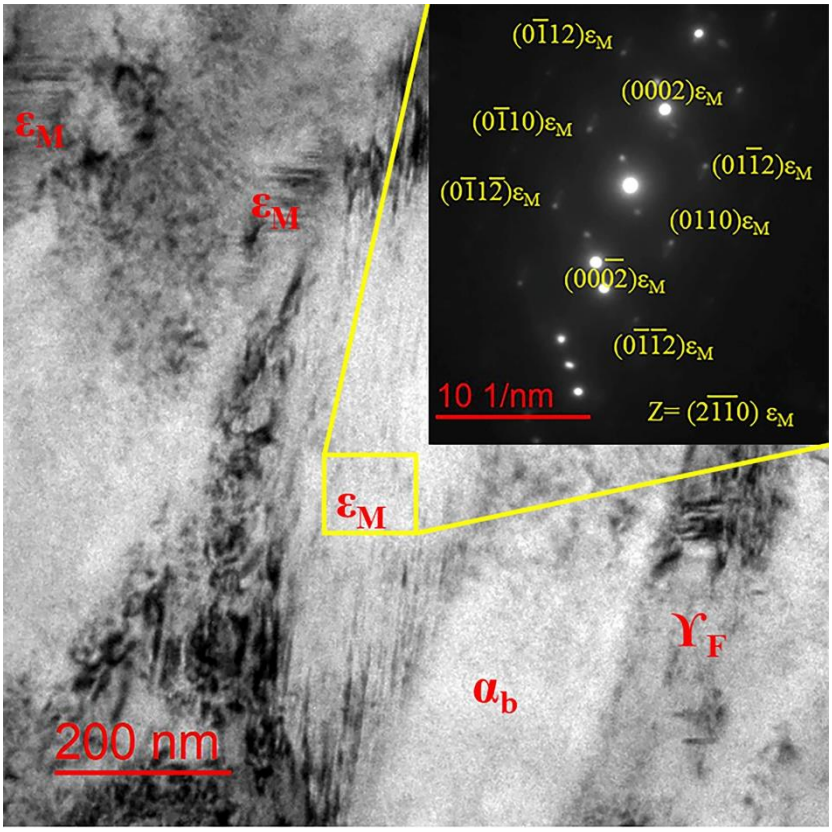

Figure 6.19 TEM BFI of sub-surface of the worn layer of B15VA-1. SAD pattern of the selected yellow coloured square area is depicted in inset. Here, ε_m, α_b and Υ_F denote epsilon martensite, bainite and filmy retained austenite, respectively.

6.6 STRAIN HARDENING EFFECTS

The microhardness at depths is measured at the cross-section of the worn surface to ensure the extent of work-hardening. Figure 6.20 depicts the microhardness variation with depth from the worn surfaces of austempered (B12VA-1, B12VA-2, B14VA-1, B14VA-2, B15VA-1 and B15VA-2) and patented steel (P12VA, P14VA and P15VA) samples after 6000 m sliding distance and normal load of 50N. It is observed that B15VA-1 sample shows greater hardened volume than the austempered and patented samples. The strain hardening effect in B15VA-1 is up to largest depth (60 μm from worn surface) and is followed by B12VA-2, B15VA-2 (40 μm from worn surface), B12VA-1, B14VA-

1, B14VA-2 (30 µm from worn surface) and patented steel samples (~25 µm from the worn surface).

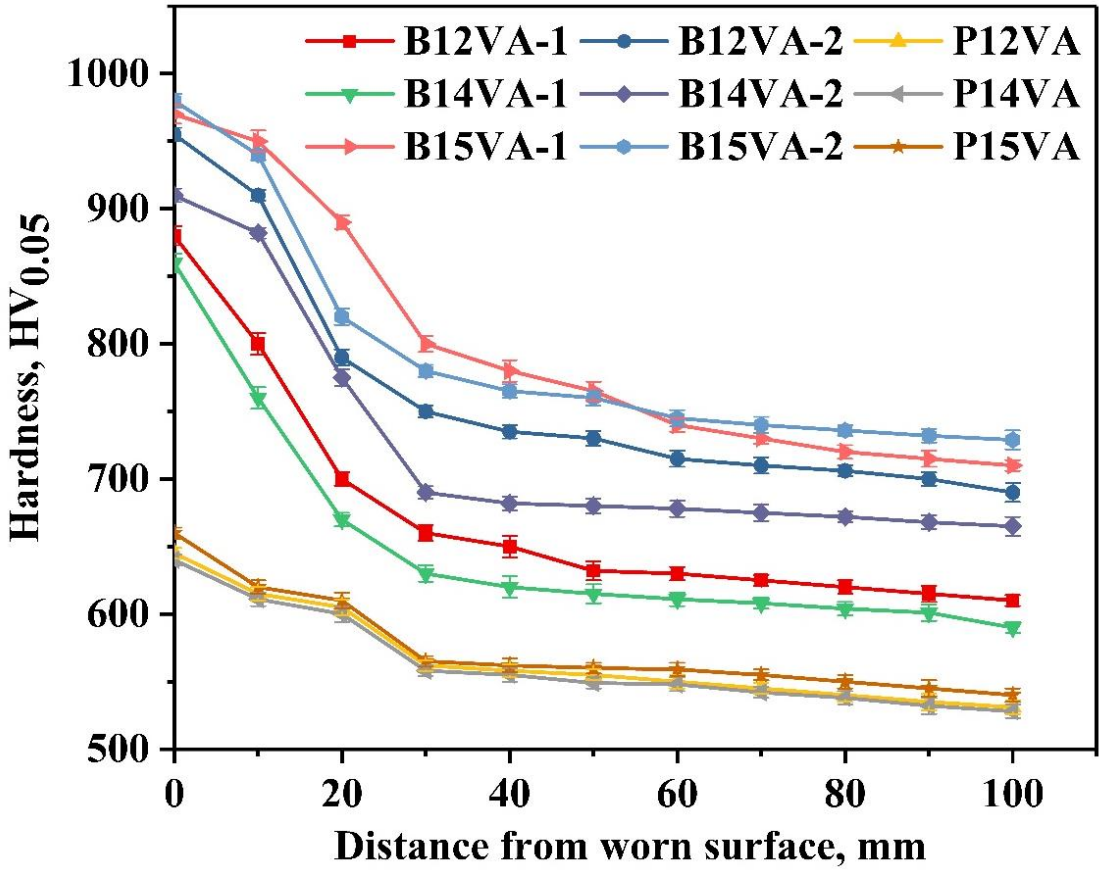

Figure 6.20 Microhardness variation with depth from the worn surfaces of austempered and patented samples after sliding distance of 6000 m at load of 50 N.

6.7 DISCUSSION

6.7.1 Tribological Behaviour

The present investigation examines the sliding wear behaviour of nanostructured bainitic and pearlitic steels subjected to pin-on-disk sliding wear on counter disc of tungsten carbide. As a consequence of the sliding of surfaces under the applied load, frictional forces and wear are produced. At the lesser load level of 10 N, it can be detected that the mass loss due to abrasion wear is fairly modest (Figure 6.1a, 6.2a, 6.3a). The slope of the line demonstrates that, as the applied load rises, the loss in mass is

significantly higher due to combined effect of abrasion and adhesive wear (Figure 6.1a-c) but the specific wear rate for the 10 N load condition is likewise the greatest. When the load increases, the specific wear rate begins to decrease, and volume loss for the sample subjected to higher load of 50 N was even less than that for 30 N loading conditions (Figure 6.6a-c). This implies that the materials are work-hardened throughout the wear, which is why material removal becomes more difficult; therefore, the removed quantity was therefore reduced. The volume loss of the materials follows the Archard's law [147]. The material B15VA-2 having higher hardness than B12VA-1, B12VA-2, B14VA-1, B14VA-2, and B15VA-1 in bainitic steel reveals lesser volume loss but the patented steel (P14VA) with least hardness (435 HV) depicts higher volume loss. As seen in Figure 6.7a-c to Figure 6.9a-c, the growth of the friction coefficient may be separated into two regimes: sharp rise and steady-state. The rapid increase in friction during the first few rotations of the pins is due to the formation of wear debris as a result of the tooling action of counter disc. Attainment of a steady-state regime in friction coefficient indicates production of a conformal contact of the steel specimen with the disc, which is corroborated by the development of grooves on the worn surface, as seen in SEM pictures. The hardness of the samples also affects the coefficient of friction [197, 198]. The CoF decreases with rising normal load for all the pins. Notable is the fact that the sample with the lowest hardness had the greatest average coefficient of friction, and vice versa. The reason for this is because a material with low hardness undergoes more plastic deformation under the same applied normal load, resulting in a bigger contact area and a greater adhesive friction [197]. A softer material is also predicted to have increased friction owing to abrasion since it carries a bigger quantity of worn debris along with the movement of the pins over the tungsten carbide counter disc.

The subsurface hardness of the pins is increased with the application of higher load. Sliding wear causes significant stresses in the material, and microstructural alignment and refinement is the key mechanism for strain accommodation. In spite of this, the ultimate microstructure of bainitic steel is dependent not only on the steadiness and amount of retained austenite, but also on the amalgamation of stresses and strains that the material endured when sliding across tungsten carbide disc. Nevertheless, the high stresses and strains turn the less carbon supersaturated blocky RA in the B15VA-1 into martensite (Figure 6.19). Blocky RA, which is abundant in B15VA-1, is more likely to strain-induced martensitic formation than film-like austenite containing more carbon, as seen in B15VA-2 [199]. The patented steel samples reveal higher hardness due to the strain hardening during the course of sliding wear at higher load. The SEM SEIs (Figure 6.12a-i), AFM (Figure 6.15a-i), and average surface roughness (Figure 6.18a-c) reveal that the smoothing of the worn surface at higher load (50 N) is due to the SIM formation in bainitic pins and strain-hardening effect in pearlitic pins.

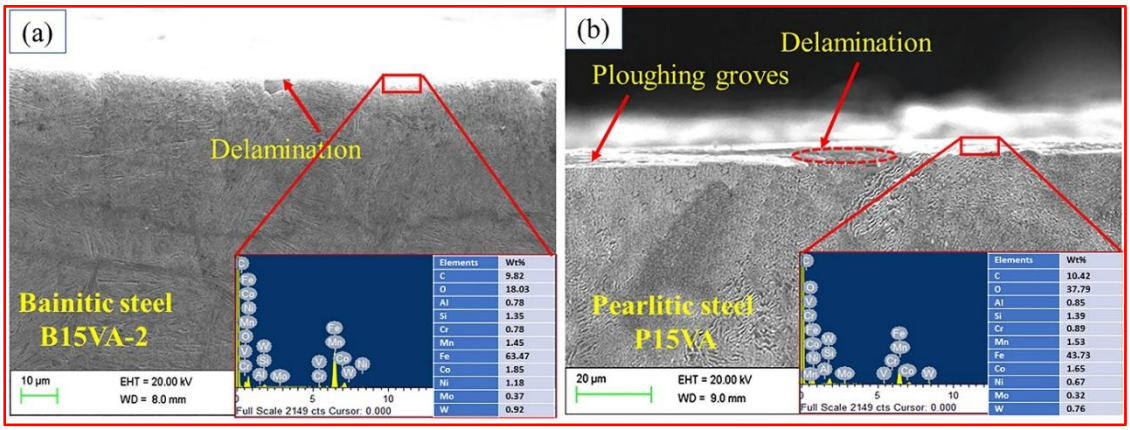

Figure 6.21 Microstructure of cross-section of worn surface of the specimen by SEM (a) bainitic steel, B15VA-2 and (b) pearlitic steel, P15VA. Energy dispersive spectroscopy analysis of marked area are shown in insets.

The cross-sectional microstructures of the worn surfaces are depicted in Figure 6.21a-b. The SEIs reveal the delamination at the worn surface in both bainitic and

pearlitic steel. Greater material loss is observed in pearlitic steel pin (Figure 6.21b). The energy dispersive spectroscopy analysis of selected area depicts that much higher amount of oxides of iron are formed in pearlitic steel pins at higher load and 6000 m sliding distance. The formation of Fe_3O_4 at lower loads and at higher load the formation of both type of Fe_3O_4 and Fe_2O_3 in wear debris during dry sliding wear is confirmed by EDS analysis, and it is in line with the literature [81, 83, 200]. The Fe_2O_3 oxide is generated at higher temperatures (or greater normal loads) and aids in avoiding metallic contact between surfaces, resulting in a mild oxidative wear regime in pearlitic steels, as described by various authors. [81, 83, 200].

6.7.2 Wear Mechanism

By analyzing the worn surface resulting from various loads and situations, two kinds of wear processes may be provided to describe the tribological behaviour of bainitic steel and three wear mechanisms for pearlitic steel obtained from the current study. As noted before, the observed wear behaviour was strongly dependent on applied load. As can be observed in Fig. 10a-i, the presence of clear wear tracks and ploughing worn debris is indicative of an abrasive wear process. Ploughing and apparent wear tracks were created, suggesting abrasive wear with an applied force of 10 N. This was because the tungsten carbide disc is significantly harder than the test samples (Figure 6.22a). With rising of the applied normal load to 50 N, delamination, material transfer and reduced ploughing grooves are revealed in the SEM SEIs. The characteristics of adhesive wear include delamination and the transfer of material, and the wear mechanism at higher loads is the result of the combined effects of abrasive and adhesive wear. During wear testing, the surface under the pin undergoes plastic deformation as a result of tangential frictional force. This occurs because the weight that is being applied to the pin rises. When

subjected to increasing loads, the connections between the test samples and the spinning disc transform into surface contacts, and materials start to adhere. As a consequence of this, transfer and delamination features are observed on the surface that has been worn. Figure 6.22b depicts the adhesive wear mechanism. Pearlitic samples reveal similar wear mechanism with an additional oxidative wear regimes formed at higher load (Figure 6.14d-f and Figure 6.21b) and temperature due to the formation of Fe_2O_3, which avoids metal to metal contact and prevent material loss (Figure 6.22c).

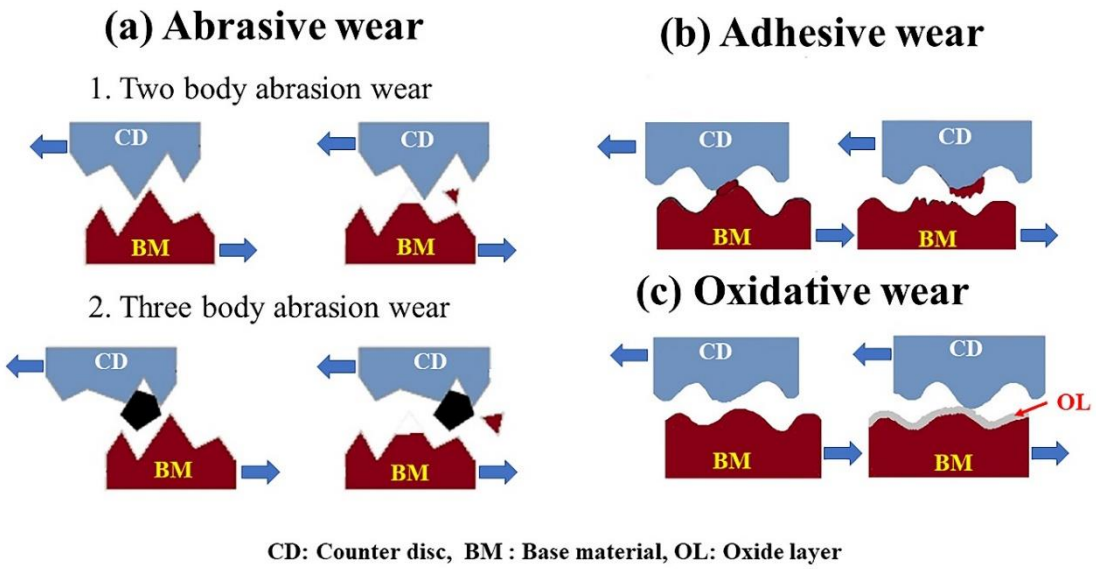

Figure 6.22 Schematic diagram showing wear mechanism in bainitic and pearlitic steels.

6.8 CONCLUSIONS

In the present investigation detailed examination of microstructure, mechanical performance and tribological behaviour of high carbon nanostructured bainitic steel, obtained by austempering at 250°C is compared with the patented steel of same composition. This investigation reveals the following significant conclusions.

1. The specific wear rate of the materials decreases with rise in applied normal load due to the formation of strain-induced martensite in bainitic pins and strain hardening effect in pearlitic steel.
2. The friction coefficient is found to decrease with increase in load due to the smoothening of the surface at higher load.
3. Blocky retained austenite of low carbon supersaturation undergoes strain-induced martensitic transformation during dry sliding wear.
4. Greater hardening volume is observed in B15VA-1 due to the effect of SIM among austempered and patented samples.
5. Worn surface morphologies at lower load (10 N) confirm the abrasive wear mechanism in all bainitic and pearlitic pins. As load increases from 10 N to 50 N the wear mechanism shifted to adhesive along with abrasive in bainitic steels. In pearlitic steel, the wear mechanisms are revealed similar to that bainitic steels along with oxidative wear.